

## **Supplementary Information**

### **Conductance measurements of polar molecules in a non-conducting solvent**

Clark Otey,<sup>†,a</sup> Mukund Sharma,<sup>†,a</sup> Jazmine Prana,<sup>a</sup> Thomas M. Czyszczon-Burton,<sup>a</sup> Alejandro Hernandez,<sup>a</sup> María Camarasa-Gómez,<sup>\*,b</sup> Daniel Hernangómez-Pérez,<sup>\*,c</sup> and Michael S. Inkpen<sup>\*,a</sup>

<sup>a</sup> Department of Chemistry, University of Southern California, Los Angeles, CA 90089, USA

<sup>b</sup> Centro de Física de Materiales (CFM-MPC) CSIC-UPV/EHU, 20018 Donostia-San Sebastián, Spain

<sup>c</sup> CIC nanoGUNE BRTA, Tolosa Hiribidea, 76, 20018 Donostia-San Sebastián, Spain

E-mail: [maria.camarasa@ehu.eus](mailto:maria.camarasa@ehu.eus), [d.hernangomez@nanogune.eu](mailto:d.hernangomez@nanogune.eu), [inkpen@usc.edu](mailto:inkpen@usc.edu)

<sup>†</sup> C.O. and M.S. contributed equally to this work.

## **Contents**

1. General Information	S2
2. Additional Conductance Data	S6
3. Additional Tunnel Coupling Calculations	S11
3. Additional Transmission Calculations	S20
4. References	S22

## 1. General Information

### Scanning Tunneling Microscope-based Break Junction (STM-BJ)

These details are reproduced here from a previous report, with only minor changes, for convenience.<sup>1</sup> Scanning tunneling microscope-based break junction (STM-BJ) measurements were performed using a custom-built STM that has been described previously.<sup>2-4</sup> Experiments were conducted at room temperature under ambient conditions. Tip–substrate distances were controlled with sub-angstrom precision using a single-axis preloaded piezoelectric actuator (P-840.1, Physik Instrumente, MA, USA). Tunneling currents were measured using a DLPCA-200 variable gain low noise transimpedance current amplifier (FEMTO Messtechnik GmbH, Berlin, Germany). Applying a voltage bias between the tip and substrate ( $V_{bias}$ ), conductance was measured as a function of tip–substrate displacement (at 40 kHz acquisition rate) as the tip was repeatedly pushed into the substrate to reach a conductance of  $>5 G_0$  (where  $G_0 = 2e^2/h$ ) and then retracted 5–10 nm (at 20 nm/s) to break the contact. The resulting conductance-distance traces were compiled into 1D conductance histograms (using 100 bins/decade along the conductance axis), or 2D conductance-distance histograms (using 100 bins/decade along the conductance axis and 1000 bins/nm along the displacement axis). Traces in 2D histograms were aligned such that displacement = 0 nm where  $G = 0.5 G_0$ . Color scales inset in 2D histograms are in count/1000 traces. Most probable conductance values for molecules studied here were obtained through Gaussian fits to their corresponding conductance peaks in 1D histograms.

STM tips were prepared from freshly cut Au wire ( $\varnothing = 0.25$  mm, 99.998%, Alfa Aesar or 99.999%, Beantown Chemical, NH, USA). Substrates were prepared from evaporation of  $>100$  nm Au (99.9985%, Alfa Aesar or 99.999%, Angstrom Engineering Inc., ON, Canada) at a rate of  $\sim 1 \text{ \AA/s}$  onto mechanically polished AFM/STM steel specimen discs (Ted Pella Inc., CA, USA) with a COVAP Physical Vapor Deposition System (Angstrom Engineering Inc., ON, Canada) used exclusively for metal evaporation. Directly before starting conductance measurements, substrates were treated with UV/ozone for 20 min (using a NovaScan PSD UV-Ozone Cleaner, Novascan Technologies, Inc., IA, USA) and used for the measurements the same day. Directly before starting measurements,  $\geq 1,000$  traces were collected to check the gold surface was free from contamination. All analytes were commercially available, and typically studied as solutions (0.1–1 mM) in isochroman (**IC**; VWR International, LLC (Ambeed),  $\geq 98\%$ ), 2,3-dihydrobenzofuran

(**DHBF**; VWR (Ambeed), 98%), dioctyl ether (**DOE**; VWR (Ambeed), 99%), or cyclopentyl methyl ether (**CPME**; Thermo Fisher Scientific Inc., >99.9%). Analyte-solvent mixtures, prepared in glass vials, were agitated in a sonic bath held at room temperature for several minutes to facilitate dissolution. All analytes and solvents were used as received without further purification.

*CAUTION: Ethereal solvents are known peroxide-forming chemicals. They should be tested for peroxide formation before distillation or evaporation, tested for peroxide formation or discarded after 1 year, or otherwise handled as otherwise directed by the supplier or recommended laboratory best practices.<sup>5</sup>*

## Computational Methods

### *Tunnel Coupling Calculations*

Density functional theory calculations (DFT) were performed using the Q-Chem 5.4.2 program, using the molecular editor and visualization package IQMol v2.15 or v3.1.<sup>6</sup> The gas phase molecular structures of each  $\alpha,\omega$ -bis(carboxylic acid) were first optimized without Au<sub>1</sub> clusters at the PBE/6-31G\*\* level of theory.<sup>7</sup> The following convergence conditions were used for all geometry optimizations (all values in atomic units [a.u.]): energy =  $20 \times 10^{-8}$ , gradient  $20 \times 10^{-6}$ ; atomic displacement =  $1200 \times 10^{-6}$ . All calculations used the direct inversion in the iterative subspace (DIIS) self-consistent field (SCF) optimization algorithm, using an on-the-fly (automated) superposition of atomic densities (AUTOSAD) initial guess. The SCF cycle was considered converged when the wave function error between consecutive SCF cycles was less than  $10^{-8}$  a.u.

The geometries of all linear  $\alpha,\omega$ -bis(carboxylic acids) (**C<sub>n</sub>**, where n = 2, 4, 6, 8, 10) were optimized with C<sub>2h</sub> symmetry imposed, whereas the geometries of **Ph**, **Cy**, and **Xy** were optimized with C<sub>2h</sub>, C<sub>i</sub>, and C<sub>s</sub>, symmetries imposed, respectively. Single gold atoms were then added, as described in the *Additional Tunnel Coupling Calculations* section below, linked to the oxygen atoms of these structures with a κ<sup>1</sup> (O-monodentate) or κ<sup>2</sup> (O,O-bidentate) coordination mode. These were then subjected to geometry optimization using the same method as before, albeit using a 6-31G\*\* basis for light atoms and LACVP for gold. After optimization, the tunnel coupling (4t<sup>2</sup>) for each Au<sub>1</sub> cluster junctions was calculated. These tunnel coupling values probe the extent of electronic coupling between Au 6s valence orbitals through a molecule, and correlate well with the experimental conductance of junctions comprising neutral linker groups (-NH<sub>2</sub>, -PR<sub>2</sub>, -SMe) with

different bridges.<sup>8–10</sup> In the present study, we utilize a negatively charged carboxylate linker, replacing  $2\times\text{H}^+$  with  $2\times\text{Au}^+$  in each  $\text{Au}_1$  cluster model to provide a charge neutral system. We therefore probe carboxylate-linked models with 2 fewer electrons than found in analogous systems with neutral linkers (which add  $2\times\text{Au}$  atoms). The relevant set of orbitals, tunnel coupled through the molecular backbone with energy splitting of  $2t$ , are therefore LUMO/LUMO+1 rather than HOMO/LUMO (see **Fig. S8** for further justification).<sup>9,11</sup> Representative isosurface plots for these frontier orbitals are provided for C4 bound to  $\text{Au}_1$  clusters (C4- $\text{Au}_1$ ) in **Figure 4**, and for all cyclic molecules in **Figure S7**.

#### *Ab initio Quantum Transport Calculations Details*

We performed *ab initio* quantum transport calculations using the combination of density functional theory (DFT) and non-equilibrium Green's function formalism (NEGF), see Ref. 12. Our DFT calculations were done employing the FHI-aims package.<sup>13</sup> Within FHI-aims, we considered the closed-shell Kohn-Sham formulation of DFT. As exchange-correlation functional, we employed the Perdew-Burke-Ernzerhof (PBE) non-empirical, generalized gradient approximation.<sup>7</sup> We incorporated scalar relativistic effects via the zeroth-order regular approximation (ZORA), which accounts for relativistic corrections to the kinetic energy.<sup>14</sup> FHI-aims employs an optimized all-electron numeric atom-centered basis set. In this work, we used the so-called “light” computational settings, which correspond approximately to double-zeta basis set quality. Our ground-state calculations were converged employing relatively strict self-consistent field (SCF) criteria: we considered our calculations to be converged only when the difference in the particle density was below  $10^{-5}$  electrons/ $\text{\AA}^3$ , the total energy change was under  $10^{-7}$  eV, and the sum of Kohn-Sham eigenvalues was below  $10^{-4}$  eV between consecutive SCF iterations. The optimized (*non-frozen*) geometries were obtained using the trust-radius-enhanced variant of the Broyden-Fletcher-Goldfarb-Shanno (BFGS) algorithm.<sup>13</sup> Structures were considered fully (structurally) relaxed when all components of the residual atomic forces fell below the threshold value of  $10^{-2}$  eV/ $\text{\AA}$ , with a force convergence threshold of  $10^{-4}$  eV/ $\text{\AA}$ .

The geometries of the model molecular junctions were determined by a well-established two-step procedure. First, for *non-frozen* geometries, we optimized the atomic positions of the molecule and the electrode tip using the methods and convergence criteria described above. This optimization was performed considering pyramidal gold clusters comprising up to 11 gold atoms per cluster. Next, the optimized molecular and tip

geometries were kept fixed, while additional gold layers were added into the outer planes of the previously optimized gold clusters. In this way, we constructed the full molecular junction, where each electrode was modeled as a pyramidal face-centered cubic (FCC) cluster of 37 atoms, cut along the (111) direction with a nearest-neighbor distance of 2.88 Å. For the *frozen* geometries, we used the molecular geometries obtained using Q-Chem for the Au<sub>1</sub>-cluster junctions, optimized as described in the *Tunnel Coupling Calculations* section, and attach directly the pyramidal cluster to build the full molecular junction without any further optimization. The size of the electrodes employed ensures screening of excess charge and accurate level alignment in the subsequent quantum transport calculations. The energy-dependent electronic transmission functions were computed using the non-equilibrium Green's function (NEGF) formalism, as implemented in the AITRANSS transport module.<sup>12,15–17</sup> The electrode self-energies were approximated using an energy-independent (Markovian) local model, given by  $\Sigma(\mathbf{r}, \mathbf{r}') = i\eta(\mathbf{r})\delta(\mathbf{r} - \mathbf{r}')$ . The local absorption rate,  $\eta(\mathbf{r})$ , was fine-tuned to ensure that the electronic transmission remained stable under smooth, moderate variations in  $\eta(\mathbf{r})$ , which is non-zero in the central subspace and is nonzero only within the outermost layers of the finite electrodes.

## 2. Additional Conductance Data

### Evaluation of Ethereal Solvents Using **bipy**

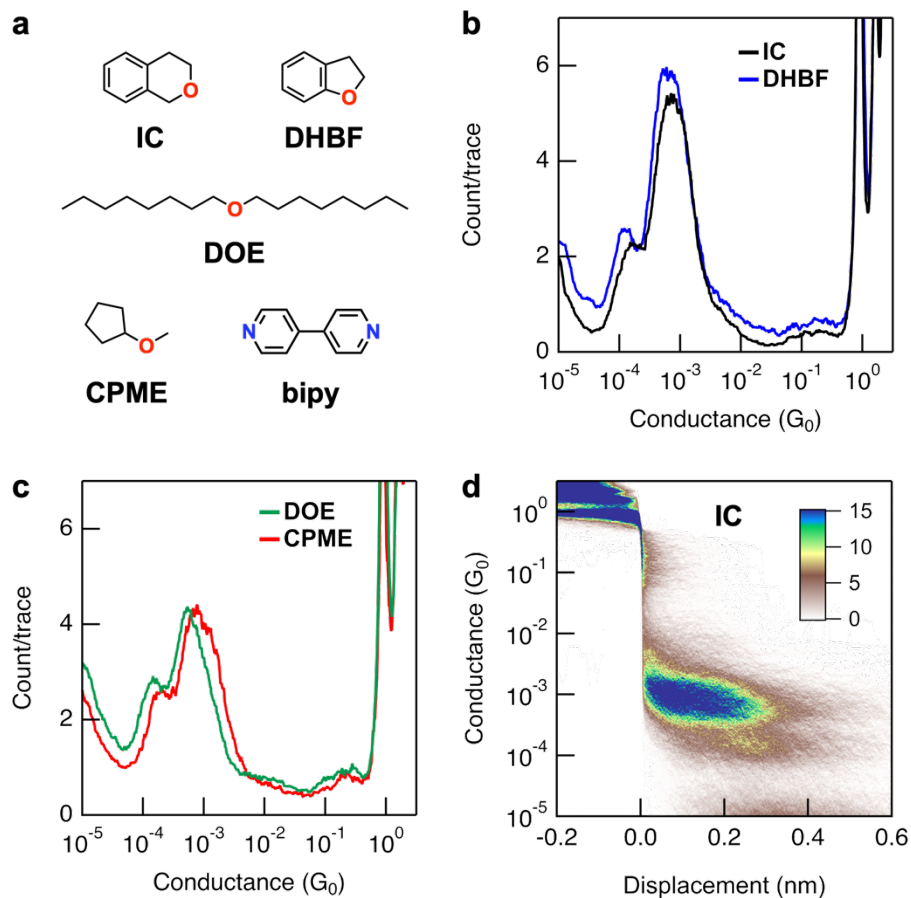


**Figure S1.** **(a)** Molecular structures of ethereal solvents isochroman (**IC**), 2,3-dihydrobenzofuran (**DHBF**), diocylether (**DOE**), and cyclopentyl methyl ether (**CPME**), as well as the model analyte 4,4'-bipyridine (**bipy**). **(b)** Overlaid 1D conductance histograms (5,000 traces,  $V_{\text{bias}} = 100$  mV) obtained for measurements of **bipy** in **IC** and **DHBF** (tetrahydrofuran analogues). **(c)** Overlaid 1D conductance histograms ( $V_{\text{bias}} = 100$  mV) for measurements of **bipy** in **DOE** (5,000 traces) and **CPME** (2,800 traces; diethyl ether analogues). We note that, due to the relatively low boiling point of **CPME**, additional drops of pure solvent must be added during experiments to compensate for evaporative losses. **(d)** A representative 2D conductance-displacement histogram for **bipy** measured in **IC**. As previously noted for studies using different high-boiling point solvents,<sup>1</sup> the similarities between conductance features obtained for all measurements suggest that the probability of **bipy** junction formation is not significantly impeded by solvent environment.

**Table S1.** Conductance histogram Gaussian peak fitting data for **bipy** junctions measured in different solvents.<sup>a</sup>

solvent	$G_{\text{bipy}} (\times 10^{-4} G_0)$		
	high	medium	low
<b>IC</b>	8.0	4.9	1.4
<b>DHBF</b>	7.4	4.5	1.2
<b>DOE</b>	6.3	4.9	1.3
<b>CPME</b>	10	5.6	1.8
TCB <sup>b</sup>	6.3	3.7	0.98
TD <sup>b</sup>	8.3	5.5	1.5

<sup>a</sup> Obtained from three peak fits to conductance histograms (**Figure S1b,c**), using the same method as previously reported by Kim *et al.*<sup>1</sup> <sup>b</sup> Previously reported conductance values for measurements in TCB (= 1,2,4-trichlorobenzene) and TD (= tetradecane) are included here for convenience. The values obtained for each ethereal solvent typically fall between or above the values obtained for TCB and TD, indicating the new solvents only weakly interact with the gold surface in the vicinity of the **bipy** junction.<sup>1,18</sup>

#### Conductance Data for $\alpha,\omega$ -Bis(Carboxylic Acid) Junctions

**Table S2.** Selected experimental conductance data for  $\alpha,\omega$ -bis(carboxylic acid) junctions.<sup>a</sup>

entry	molecule	conductance ( $G_0$ ) <sup>b</sup>
1	<b>C2</b>	$1.17 \times 10^{-3}$
2	<b>C4</b>	$2.00 \times 10^{-4}$
3	<b>C6</b>	$3.43 \times 10^{-5}$
4	<b>C8</b>	$5.35 \times 10^{-6}$
5	<b>Ph</b>	$1.35 \times 10^{-4}$
6	<b>Cy</b>	$1.31 \times 10^{-4}$
7	<b>Xy</b>	$1.22 \times 10^{-4}$

<sup>a</sup> Conductance values obtained from Gaussian fits to the lowest conductance peak observed in each of the 1D conductance histograms shown in **Figure 2** and **3**. <sup>b</sup> The conductance values obtained here are in good agreement with conductance features reported previously for **Cn** junctions formed from aqueous or toluene solutions.<sup>19,20</sup>

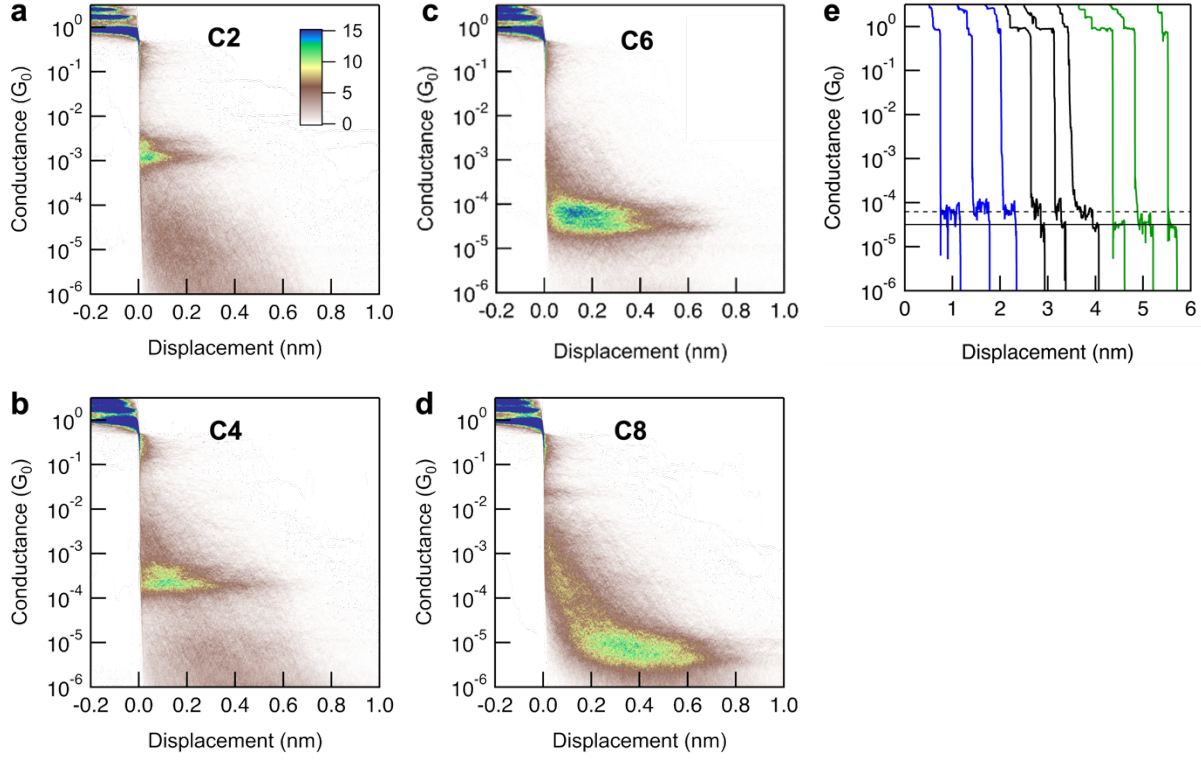


**Figure S2.** 2D conductance-displacement histograms corresponding to the 1D conductance histograms shown in **Figure 2** for (a) C2, (b) C4, (c) C6 (reproduced from **Figure 2b** for convenience) and (d) C8. (e) Selected conductance-displacement traces for C6 junctions, illustrating conductance features that show: (i) an isolated high-conductance step (blue); (ii) a break from a high conductance step to a low conductance step (black); (iii) an isolated low-conductance step (green). Dashed and solid horizontal lines highlight the most probable conductance of high and low conductance features, respectively. While these example traces offer additional support for the expected transitions from the hypothesized two-molecule to one-molecule junction geometries, we note that a continuum of step features spanning these extremes can be identified in conductance-displacement traces within this C6 dataset.

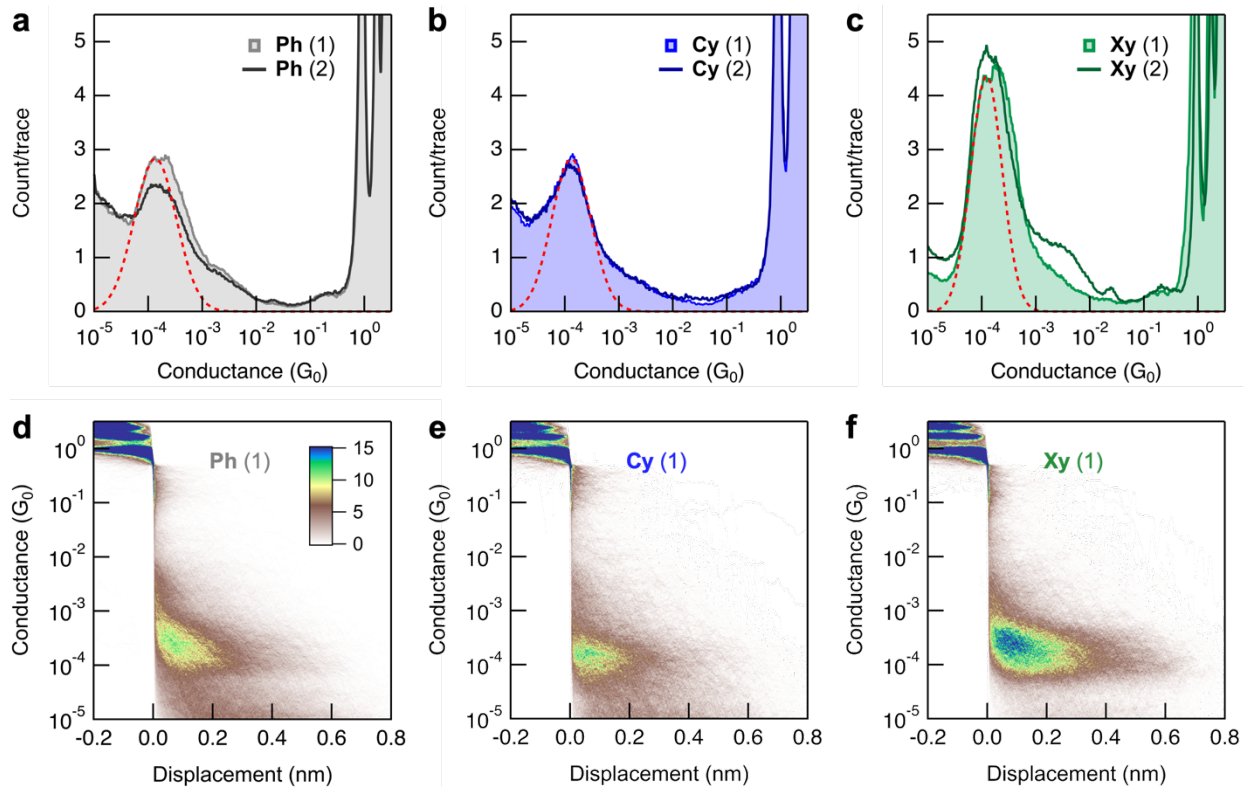


**Figure S3.** Overlaid 1D conductance histograms for repeated measurements of **(a) Ph**, **(b) Cy**, **(c) Xy** (5,000-10,000 traces,  $V_{bias} = 250$  mV). The data presented here for **Ph** is obtained from measurements of apparently saturated solutions after sonication at room temperature (<0.5 mM). However, **Ph** is observed to fully dissolve to form ~1 mM solutions when sonicated at elevated temperatures (~40°C). Measurements of these higher concentration solutions provide 1D conductance histograms that appear dominated by conductance features corresponding to two molecule junctions (not shown). **(d-f)** Representative 2D conductance-displacement histograms corresponding to the solid 1D histograms shown in panels (a-c).

### *Additional Measurements of C0 and C6*

While solutions of ethanedioic acid (**C0**) can also be prepared in **IC** (at least to  $\sim$ 0.5 mM), no clear junction features are observed in STM-BJ studies. We attribute this to the short length of **C0**, which will provide only small step features in conductance traces and could also reduce the probability of molecular junction formation.<sup>21</sup> Analysis of 2D histograms reveals that the maximum displacement of **Cn** junctions decreases by 1-2 Å as n is reduced by 2, and that **C2** junctions typically extend to a displacement of  $\sim$ 2 Å (**Figures 2b** and **S2**). Notably, this result contrasts with previous studies, for example, on silver and copper electrodes, which have observed conductance features in measurements of **C0**.<sup>22</sup>

For completeness, we report that a conductance peak for **C6** can be obtained from an analyte-coated substrate after drop casting a  $\sim$ 20 mM solution in tetrahydrofuran (THF, **Figure S4**). However, we find this method of introducing junction components to be less consistent than solution studies which provide greater control over the local concentration of analyte molecules near the junction. Notably, conductance studies of **C6** as a saturated solution in 1,2,4-trichlorobenzene (TCB) provided only broad, ill-defined conductance features, further highlighting the utility of **IC** for STM-BJ measurements of polar analytes.

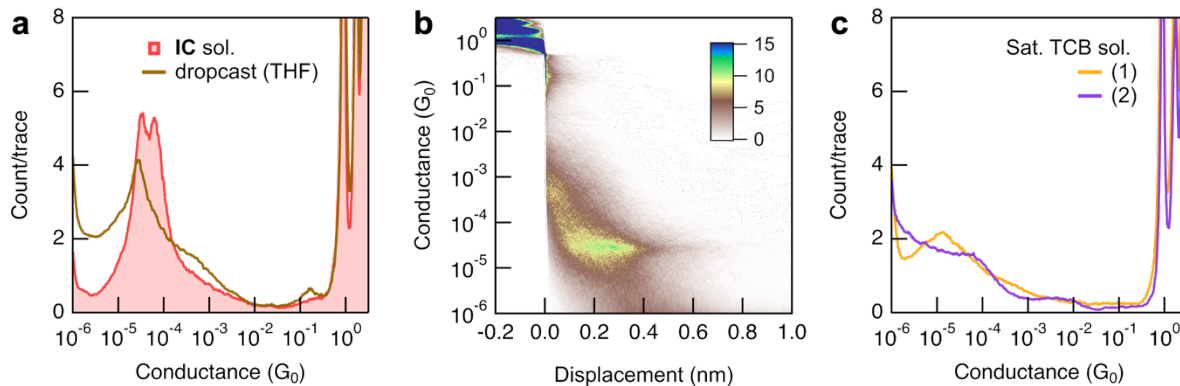


**Figure S4.** (a) Overlaid 1D conductance histograms for **C6**, obtained from measurements of an **IC** solution (reproduced from **Figure 2** for convenience) or an analyte-coated substrate after drop casting a  $\sim$ 20 mM solution in THF. (b) 2D histogram corresponding to the drop cast conductance data from panel (a). (c) Overlaid 1D conductance histograms from repeated measurements of a saturated solution of **C6** in TCB show only inconsistent, ill-defined conductance features.

### 3. Additional Tunnel Coupling Calculations

#### *Geometry Optimization of C<sub>n</sub>-Au<sub>1</sub> Junctions ( $\kappa^1$ Coordination)*

We first explored the impact of starting Au-O bond lengths and Au-O-C bond angles on the optimized geometries of **C2-Au<sub>1</sub>** and **C4-Au<sub>1</sub>** cluster junctions. To construct input structures, we replaced the carboxylic acid protons of the geometry-optimized parent  $\alpha,\omega$ -bis(carboxylic acid) molecular structures with single gold atoms. Guided by the X-ray crystal structure of acetato(triphenylphosphine)gold(I) ( $\text{Ph}_3\text{PAuOCOCH}_3$ ),<sup>23</sup> we initially set Au-O = 2.063 Å and Au-O-C = 87.26°. After geometry optimization, we obtained  $\kappa^1$  coordination modes for both junctions (for **C4** calculations involving constrained  $\kappa^2$  coordination geometries, see below). However, the resulting Au-O bond lengths and Au-O-C angles proved significantly different from each other (entries 1-2, **Table S3**). Notably, the contact geometry of **C4-Au<sub>1</sub>** did not change significantly if optimization was performed from an input structure with the larger bond lengths and angles of the geometry-optimized **C2-Au<sub>1</sub>** junction (entry 3a, **Table S3**). Given that a longer Au-O bond and more obtuse Au-O-C angle would favor optimization to the observed  $\kappa^1$  coordination mode, important for consistency across our tunnel coupling calculations (see below), we used Au-O ~ 2.2 Å and Au-O-C ~ 95° for all subsequent input geometries. We attribute the differences between our computed  $\kappa^1$  contact geometries and the  $\kappa^1$  geometry observed in the experimental X-ray crystal structure to the absence of Au-coordinated PPh<sub>3</sub>, and/or the close-packed molecular crystal environment, in our calculations.

To evaluate the different contact geometries obtained for **C2-Au<sub>1</sub>** and **C4-Au<sub>1</sub>** cluster junctions, we performed analogous geometry-optimization calculations for junctions with n = 6, 8, 10. Here we find the Au-O bonds (2.061-2.133 Å) and Au-O-C angles (103.94-108.78°) are broadly consistent with those obtained for **C4-Au<sub>1</sub>**. Accordingly, we propose **C2-Au<sub>1</sub>** is an outlier in our calculations due to the short alkane backbone and corresponding proximity of terminal -COOAu groups. The comparable contact geometries for **C<sub>n</sub>-Au<sub>1</sub>** junctions with n = 4-10 facilitate the observation of clear trends between tunnel coupling and molecular length as presented in **Figure 4**. Notably, all **C<sub>n</sub>-Au<sub>1</sub>** junctions have a C-O-C-C dihedral angle,  $\beta$ , = 180° (**Figure S5**).

#### *Geometry Optimization of Au<sub>1</sub> Junctions with Cyclic Backbones*

The geometries of **Ph-Au<sub>1</sub>**, **Cy-Au<sub>1</sub>**, and **Xy-Au<sub>1</sub>** junctions were optimized using the same method as described above for **C<sub>n</sub>-Au<sub>1</sub>** junctions. However, we note that the orientation of the AuOC(O)-

linker relative to each backbone is distinct, which complicates direct comparison of their calculated tunnel couplings (and transmission at the Fermi level,  $E_F$ ). This issue is moderated by recognizing that the energy barriers to rotation about the AuOC(O)-aryl, AuOC(O)-cyclohexyl, CH<sub>2</sub>-aryl, or AuCOO-CH<sub>2</sub> bonds are expected to be modest relative to the thermal energy at room temperature. As a result, we will sample a range of contact configurations during experimental conductance measurements. By calculating tunnel couplings for different geometries, we can obtain insights into their relative influence on junction conductance.<sup>10,11</sup>

**Table S3.** Selected structural parameters of Au<sub>1</sub> cluster junctions.<sup>a</sup>

entry	molecule	dihedrals (°) <sup>b</sup>		Au-O (Å)	Au-O-C (°)	Au-Au (Å)	symmetry
		input	optimized				
1 <sup>c</sup>	<b>C2</b>	$\beta = 180$	$\beta = 180$	2.231	95.38	9.213	C <sub>2h</sub>
2 <sup>c</sup>	<b>C4</b>	$\beta = 180$	$\beta = 180$	2.062	108.40	11.993	C <sub>2h</sub>
3a	<b>C4</b>	$\beta = 180$	$\beta = 180$	2.061	108.48	11.996	C <sub>2h</sub>
3b	<b>C4</b>	$\beta = 180$	$\beta = 180$	2.320 <sup>d</sup>	89.265, 89.313	11.487	C <sub>s</sub>
4	<b>C6</b>	$\beta = 180$	$\beta = 180$	2.061	108.78	14.563	C <sub>2h</sub>
5	<b>C8</b>	$\beta = 180$	$\beta = 180$	2.133	103.94	17.000	C <sub>2h</sub>
6	<b>C10</b>	$\beta = 180$	$\beta = 180$	2.132	104.43	19.575	C <sub>2h</sub>
7	<b>Ph</b>	$\alpha = 0$	$\alpha = 0$	2.096	103.60	11.152	C <sub>2h</sub>
8	<b>Ph</b>	$\alpha = 90$ <sup>e</sup>	$\alpha = 90$ <sup>e</sup>	2.138	105.32	11.194	C <sub>i</sub>
9	<b>Cy</b>	$\beta = 180$	$\beta = 154.65$	2.137	106.33	11.406	C <sub>i</sub>
10	<b>Cy</b>	$\beta = 135$	$\beta = 113.14$	2.123	109.01	11.474	C <sub>i</sub>
11	<b>Cy</b>	$\beta = 90$	$\beta = 124.81$	2.123	108.97	11.474	C <sub>i</sub>
12	<b>Xy</b>	$\gamma = 90,$ $\delta = 180$	$\gamma = 90,$ $\delta = 180$	2.243	95.010	12.370 <sup>f</sup>	C <sub>2h</sub>
13	<b>Xy</b>	$\gamma = 0,$ $\delta = 180$	$\gamma = 0,$ $\delta = 180$	2.126	105.683	13.449 <sup>f</sup>	C <sub>2h</sub>
14	<b>Xy</b>	$\gamma = 90,$ $\delta = 90$	$\gamma = 57.12,$ $\delta = 119.61$	2.134	106.693	12.742 <sup>f</sup>	C <sub>i</sub>
15	<b>Xy</b>	$\gamma = 0,$ $\delta = 90$	$\gamma = 58.38,$ $\delta = 108.07$	2.143	104.750	12.281 <sup>f</sup>	C <sub>i</sub>

<sup>a</sup> Optimized with starting geometries having Au-O ~ 2.2 Å and Au-O-C = 95°, unless stated.<sup>b</sup> Angles defined in **Figure S5**. <sup>c</sup> Optimized with starting geometries having Au-O = 2.063 Å and Au-O-C = 87.27° (cells shaded red). <sup>d</sup> Optimized with Au-O bond lengths constrained to 2.320 Å ( $\kappa^2$  coordination mode). <sup>e</sup> Optimized using constrained dihedral angles. <sup>f</sup> The ~1 Å larger Au-Au distances for **Xy-Au<sub>1</sub>** relative to **Ph-Au<sub>1</sub>/Cy-Au<sub>1</sub>** correlates well with the larger step lengths observed for these junctions in 2D conductance-displacement histograms (**Figure 3d-f**).

Accordingly, we performed geometry optimizations for **Ph-Au<sub>1</sub>**, **Cy-Au<sub>1</sub>**, and **Xy-Au<sub>1</sub>** junctions starting from a set of different dihedral angles noted in **Table S3** and defined in **Figure S5**. The optimized dihedral angles resulting from each calculation, corresponding to molecular configurations with local energy minimums, are also listed in **Table S3** and further illustrated in **Figure S6**. Here, we constrained  $\alpha = 90^\circ$  for **Ph-Au<sub>1</sub>** to avoid the geometry relaxing back to  $\alpha = 0^\circ$  (providing one additional geometry for comparison). We note that all contact geometries, except for **Xy-Au<sub>1</sub>** with  $\gamma = 90^\circ$ ,  $\delta = 180^\circ$  (entry 12, **Table S3**), provided Au-O bonds (2.096-2.143 Å) and Au-O-C angles (103.60-109.01°) close to the values obtained for **C<sub>n</sub>-Au<sub>1</sub>** ( $n = 4-10$ ). The consistency of these  $\kappa^1$  contact geometries indicates their use to evaluate the influence of dihedral angles on tunnel couplings is reasonable.

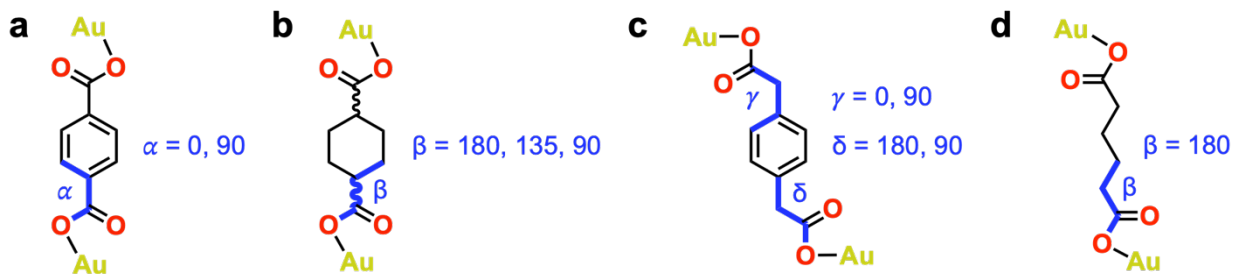
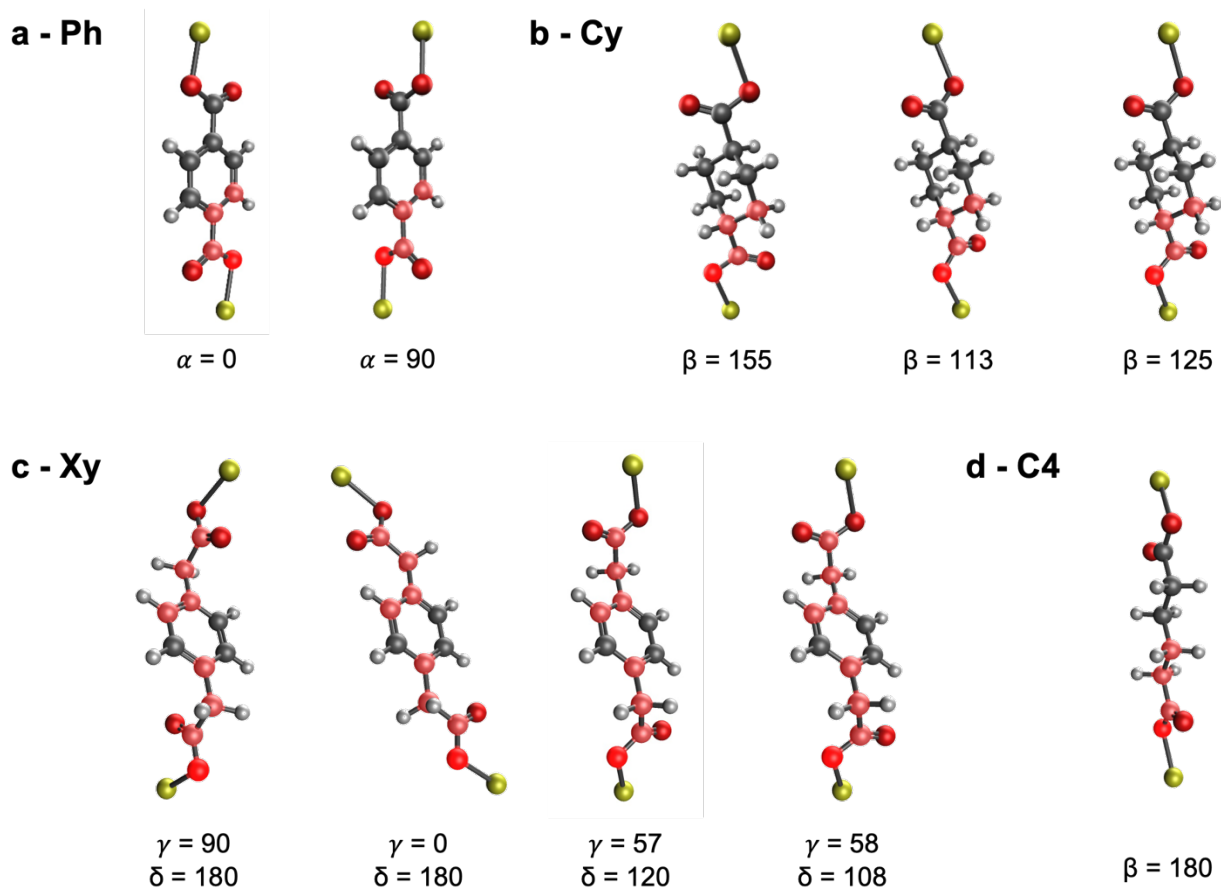


**Figure S5.** Molecular structures highlighting the atoms used to define each dihedral angle (connected by blue solid bonds) for (a) **Ph-Au<sub>1</sub>**, (b) **Cy-Au<sub>1</sub>**, (c) **Xy-Au<sub>1</sub>**, (d) **C4-Au<sub>1</sub>**. Angles listed are those utilized in the input structures noted in **Table S3**. Molecular structures of optimized geometries are provided in **Figure S6**.



### Tunnel Coupling Calculations

Tunnel couplings for each Au<sub>1</sub> junction geometry, which are related to their conductance,<sup>8–10,24</sup> are provided in **Table S4**. The ratio of calculated  $4t^2_{\max}/4t^2_{\min}$  for each cyclic junction is <1 order of magnitude (**Ph** = 3.6, **Cy** = 7.0, **Xy** = 7.3). This range is well within the approximate width of the experimental conductance peaks observed in **Figure 3** for junctions with cyclic bridge groups. However, additional calculations are required to evaluate the relative probabilities of forming each junction geometry, and to establish if a specific geometry (or geometries) may dominate during experimental measurements. The width of conductance peaks is expected to be further broadened by differences in the contact geometry ( $\kappa^1$  or  $\kappa^2$ , discussed further below; entries 3a and 3b, **Table S4**), as well as the electrode geometry involved in forming the contact,<sup>25</sup> from junction to junction.

**Table S4.** Selected electronic parameters for Au<sub>1</sub> cluster junctions.<sup>a</sup>

entry	molecule	optimized dihedrals (°) <sup>b</sup>	$4t^2$ (eV)
3a	<b>C4</b>	$\beta = 180$	$4.98 \times 10^{-3}$
3b <sup>c</sup>	<b>C4</b>	$\beta = 180$	$1.43 \times 10^{-3}$
4	<b>C6</b>	$\beta = 180$	$9.17 \times 10^{-4}$
5	<b>C8</b>	$\beta = 180$	$1.42 \times 10^{-4}$
6	<b>C10</b>	$\beta = 180$	$2.98 \times 10^{-5}$
7	<b>Ph</b>	$\alpha = 0$	$1.10 \times 10^{-3}$
8	<b>Ph</b>	$\alpha = 90$	$3.92 \times 10^{-3}$
9	<b>Cy</b>	$\beta = 154.65$	$3.04 \times 10^{-4}$
10	<b>Cy</b>	$\beta = 113.14$	$2.12 \times 10^{-3}$
11	<b>Cy</b>	$\beta = 124.81$	$2.12 \times 10^{-3}$
12	<b>Xy</b>	$\gamma = 90, \delta = 180$	$9.66 \times 10^{-4}$
13	<b>Xy</b>	$\gamma = 0, \delta = 180$	$7.28 \times 10^{-4}$
14	<b>Xy</b>	$\gamma = 57.12, \delta = 119.61$	$5.35 \times 10^{-3}$
15	<b>Xy</b>	$\gamma = 58.38, \delta = 108.07$	$4.44 \times 10^{-3}$

<sup>a</sup> Angles defined in **Figure S6**. Green shaded rows correspond to junction geometries with the largest tunnel coupling(s) for each of the cyclic molecular backbones. <sup>c</sup> Optimized with Au-O bond lengths constrained to 2.320 Å ( $\kappa^2$  coordination mode).

The apparent influence of changing dihedral angles on the highest and lowest calculated tunnel couplings, for **Ph-Au<sub>1</sub>**, **Cy-Au<sub>1</sub>**, and **Xy-Au<sub>1</sub>** junctions, can be briefly summarized (for isosurface plots, see **Figure S7**). For **Ph-Au<sub>1</sub>**,  $\alpha = 0^\circ$  aligns the Au-O and C-O bonds parallel to the plane of the aromatic ring (minimizing electronic coupling into the delocalized  $\pi$ -system).

When  $\alpha = 90^\circ$ , orientation of the Au-O-C motif above and below the phenyl plane improves coupling between the linker and phenyl bridge (likely through the proximal gold-bound O 2p orbital). Corroborating these arguments, we find, in **Figure S7**, that the LUMO+1 exhibits a larger orbital density on the backbone atoms for the  $\alpha = 90^\circ$ , relative to the  $\alpha = 0^\circ$ , **Ph** junction geometry. For **Cy-Au<sub>1</sub>**,  $\beta = 180^\circ$  aligns the Au-O bond of each AuOC(O)- linker with one of two alkane branches of the cyclic backbone in an all-*trans* configuration. Interestingly, an improved tunnel coupling is observed for geometries where  $\beta \neq 180^\circ$ . The influence of possible destructive  $\sigma$ -interference effects<sup>26</sup> that may manifest in this cyclic alkane are also described below. For **Xy**, geometries with  $\gamma = 0$ ,  $\delta = 180^\circ$  again align the Au-O and C-CH<sub>2</sub> bonds parallel to the plane of the aromatic ring, resulting in a lower tunnel coupling. In contrast, input geometries with  $\delta = 90^\circ$  ( $\gamma = 90$  or  $0^\circ$ ) converge to a similar configuration ( $\delta = 108\text{-}120^\circ$ ,  $\gamma = 57\text{-}58^\circ$ ), which improves alignment of the Au-O-C-CH<sub>2</sub> group with the backbone  $\pi$ -system, providing an increased tunnel coupling.

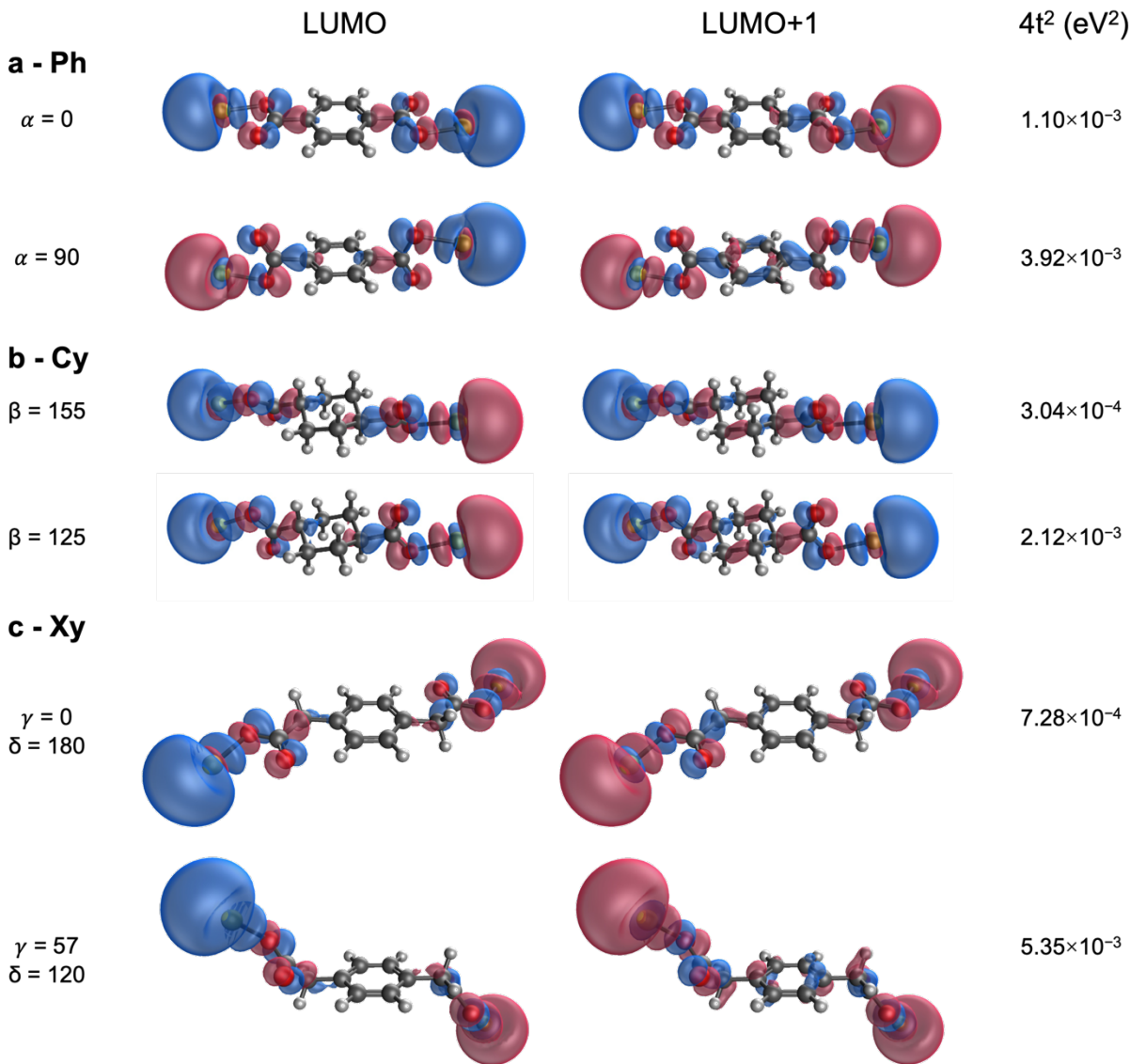


**Figure S7.** Isosurface plots (isovalue =  $0.06 \text{ \AA}^{-3}$ ) of the DFT-calculated LUMO and LUMO+1 orbitals for (a) Ph-Au<sub>1</sub>, (b) Cy-Au<sub>1</sub>, and (c) Xy-Au<sub>1</sub> junction geometries that provide the highest and lowest tunnel couplings for each cyclic bridge. Analogous pairs of symmetric and antisymmetric orbitals have been observed in earlier studies of dative linker-gold contacts.<sup>27</sup> These plots illustrate how the Au *s* orbitals are tunnel coupled through a given molecular backbone. Notably, a larger orbital density on each bridge group is observed in the LUMO+1 for the geometries that exhibit larger tunnel couplings.

#### *Calculations for C4-Au<sub>1</sub> Junctions with $\kappa^2$ Coordination*

For completeness, we also optimized the geometry of C4-Au<sub>1</sub> after constraining all Au-O bond lengths to 2.320 Å ( $\kappa^2$  coordination mode; entry 3b, **Table S3**). This Au-O bond length was

intermediate between the bond lengths observed for  $\kappa^2$ -coordinated carboxylic acids in fully relaxed junctions with  $\text{Au}_{37}$  clusters (see below). Notably, the calculated Au-Au distance is smaller for the **C4-Au<sub>1</sub>( $\kappa^2$ )** junction (**Table S3**), and the calculated tunnel coupling for **C4-Au<sub>1</sub>( $\kappa^2$ )** is 3.5-times smaller than for **C4-Au<sub>1</sub>( $\kappa^1$ )** (**Table S4**). This result further supports our hypothesis that the high and low conductance peaks observed most prominently in **Cn** measurements correspond to junctions comprising one- or two-molecules, rather than to a systematic change in coordination geometry with junction displacement. Specifically, we do not frequently observe conductance features consistent with changes from shorter, lower conductance **Cn-Au<sub>1</sub>( $\kappa^2$ )** junctions to longer, higher conductance **Cn-Au<sub>1</sub>( $\kappa^1$ )** junctions with increasing tip-substrate displacement. Furthermore, the tunnel coupling and transmission calculations (**Figure 4c**) presented here show that changes in the coordination mode of carboxylate junctions result in relatively small changes in conductance (less than a factor of 4), even when the coordination mode of both linkers are varied simultaneously. This is consistent with the results of earlier work which found that changing the coordination mode of one carboxylate linker resulted in only small changes in calculated conductance.<sup>28</sup> Taken together, we suggest that while both coordination modes may be accessed experimentally, the sampling of these different junction geometries are not expected to provide discreet peak features but are likely to contribute to the widths of the conductance peaks observed.

### *Outlook*

The analysis presented here extends our understanding of how electrode-linker geometry may influence charge transport through molecular junctions. For example, in junctions comprising oligoaryl backbones with directly connected electrode linkers such as -NH<sub>2</sub>, -SMe, or -SH, the resulting gold-linker bond can adopt energetically-accessible configurations in which it is oriented parallel to the *p*-orbitals of the backbone  $\pi$ -system.<sup>10</sup> However, it has been recognized that this electronic coupling can be reduced by changing the orientation of the electrode-linker bond,<sup>11,29</sup> or by changing the placement of the linker on the backbone.<sup>30</sup> As evidenced here, carboxylic acid groups fall into a distinct category of linkers that appear to exhibit unique relationships between electrode-backbone coupling and geometry which warrant additional investigation.

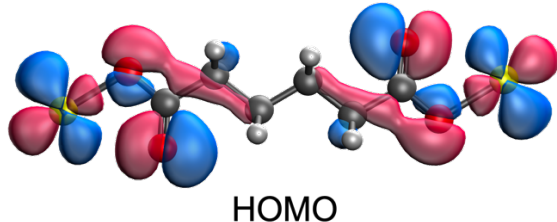


**Figure S8.** Isosurface plots (isovalue =  $0.06 \text{ \AA}^{-3}$ ) of the DFT-calculated HOMO orbital for  $\text{C4-Au}_1$ . The distinct orbital symmetry of this orbital relative to the LUMO and LUMO+1 (**Figure 4a**), involving gold  $d$ -orbital rather than  $s$ -orbital character, further justifies the selection of the LUMO and LUMO+1 orbitals for tunnel coupling calculations using the carboxylate-linked models studied here (see *Computational Methods* for primary discussion). We emphasize here that our choice of LUMO and LUMO+1 reflects the charge neutral nature of the  $\text{Au}_1$  model junctions analyzed, in which the carboxylate linkers each have a formal charge of  $1^-$  and the gold atoms have a formal charge of  $1^+$ . If two electrons are added to the system, providing a  $[\text{C4-Au}_1]^{2-}$  model that formally comprises  $\text{Au}(0)$  atoms, then the tunnel coupled orbitals exhibit the same form as shown in **Figure 4a** but are now designated as HOMO and LUMO (as confirmed through control calculations, not shown). We stress that the choice of orbitals used to evaluate electronic coupling through a molecular backbone is guided by the form of the orbitals and not their specific orbital occupancy/designation. This is nicely illustrated in work by Klausen *et al.*,<sup>31</sup> in which the electronic coupling through different backbones was evaluated using energy differences between the HOMO and HOMO-1 of isolated molecules in the gas phase. In this case, the calculated energy differences reflected the extent of electronic interactions between distal sulfur lone pairs.

## 4. Additional Transmission Calculations

We plot, in **Figure S9**, overlaid transmission calculations for **C4**, **Ph**, **Cy**, and **Xy** junctions with fully relaxed geometries. These geometries, obtained using the methodology presented in the *Computational Methods* section, are provided in **Figure S10**. Upon geometry optimization, we find that some contact configurations change from  $\kappa^1$  to  $\kappa^2$  coordination mode (or mixed  $\kappa^1/\kappa^2$ ), exhibiting additional Au-O bonding. The additional Au-O bonding arises from the strong Lewis basicity of oxygen and the electron-accepting nature of gold, which facilitates the formation of such bonds when the geometry and charge distribution allows for it upon symmetry-unconstrained relaxation. Consequently, we observe changes in conductance, which result from a combination of modified level alignment and variations in the HOMO-LUMO gap.

Two observations are now in order: First, we observe a conductance trend **C4** > **Cy**, **Xy** > **Ph** that closely follows the one observed in experiments (**C4** > **Ph**, **Cy**, **Xy**); second, the HOMO-LUMO gap is reduced for **Ph** junctions relative to the frozen geometry. This reduction can be attributed to the increased conjugation between the  $\pi$ -backbone and the carboxylate linkers when these are co-planar. Despite the contact coordination and backbone geometric changes upon full relaxation, all molecular junctions remain HOMO-conducting with pinning to the  $E_F$ , as was the case with the “frozen” geometries (we easily identify the HOMO from the gas-phase molecular HOMO-LUMO gap, **Table S5**). Due to the strong charge transfer between the charged carboxylate linker and the gold electrode, the geometric changes have a limited influence on the conductance properties of these junctions.

Interestingly, we note that **Cy** exhibits an apparent mid-gap antiresonance, consistent with previous observations of destructive  $\sigma$ -interference effects in structurally similar cyclic alkanes.<sup>26</sup> In our calculations, however, this feature occurs away from  $E_F$ , and does not significantly influence junction transmission relative to the linear **C4** analogue.

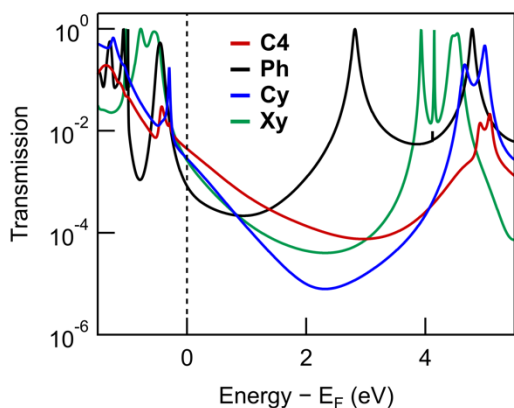


**Figure S9.** Additional transmission calculations for **C4**, **Ph**, **Cy**, and **Xy** junctions with fully relaxed geometries (geometries provided in **Figure S10**).

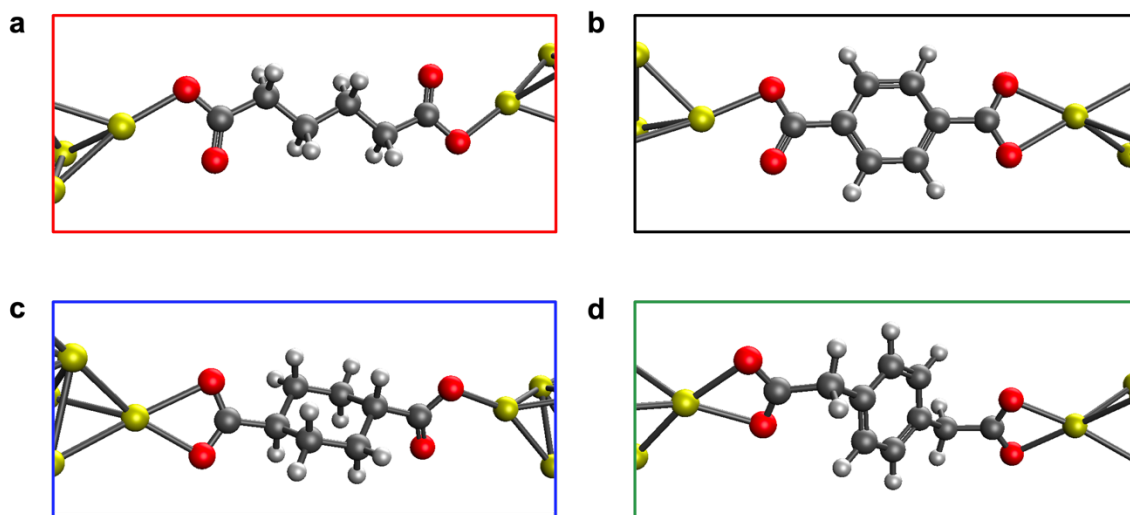


**Figure S10.** Fully relaxed geometries for (a) **C4**, (b) **Ph**, (c) **Cy**, and (d) **Xy** junctions, used for the transmission calculations presented in **Figure S9**.

**Table S5.** Selected data for transmission calculations.

molecule	geometry	HOMO-LUMO gap (eV) <sup>a</sup>	calc. G ( $G_0$ ) <sup>b</sup>
<b>C4</b> ( $\kappa^1$ )	frozen	-	$7.4 \times 10^{-3}$
<b>C4</b> ( $\kappa^2$ )	frozen	-	$2.7 \times 10^{-3}$
<b>C4</b>	relaxed	5.36	$4.4 \times 10^{-3}$
<b>Ph</b>	frozen	-	$2.9 \times 10^{-2}$
<b>Ph</b>	relaxed	3.52	$8.1 \times 10^{-4}$
<b>Cy</b>	frozen	-	$9.7 \times 10^{-3}$
<b>Cy</b>	relaxed	5.08	$2.8 \times 10^{-3}$
<b>Xy</b>	frozen	-	$2.3 \times 10^{-2}$
<b>Xy</b>	relaxed	4.24	$2.6 \times 10^{-3}$

<sup>a</sup> Obtained from gas phase optimized molecules. <sup>b</sup> Obtained from the transmission at  $E_F$ .

## 5. References

- (1) Kim, L.; Czyszczon-Burton, T. M.; Nguyen, K. M.; Stukey, S.; Lazar, S.; Prana, J.; Miao, Z.; Park, S.; Chen, S. F.; Inkpen, M. S. Low Vapor Pressure Solvents for Single-Molecule Junction Measurements. *Nano Lett.* **2024**, *24* (32), 9998–10005.
- (2) Miao, Z.; Quainoo, T.; Czyszczon-Burton, T. M.; Rotthowe, N.; Parr, J. M.; Liu, Z.; Inkpen, M. S. Charge Transport across Dynamic Covalent Chemical Bridges. *Nano Lett.* **2022**, *22* (20), 8331–8338.
- (3) Venkataraman, L.; Klare, J. E.; Tam, I. W.; Nuckolls, C.; Hybertsen, M. S.; Steigerwald, M. L. Single-Molecule Circuits with Well-Defined Molecular Conductance. *Nano Lett.* **2006**, *6* (3), 458–462.
- (4) Inkpen, M. S.; Liu, Z.; Li, H.; Campos, L. M.; Neaton, J. B.; Venkataraman, L. Non-Chemisorbed Gold–Sulfur Binding Prevails in Self-Assembled Monolayers. *Nature Chem.* **2019**, *11*, 351–358.
- (5) Clark, D. E. Peroxides and Peroxide-Forming Compounds. *Chem. Health Saf.* **2001**, *8* (5), 12–22.
- (6) Epifanovsky, E.; Gilbert, A. T. B.; Feng, X.; Lee, J.; Mao, Y.; Mardirossian, N.; Pokhilko, P.; White, A. F.; Coons, M. P.; Dempwolff, A. L.; Gan, Z.; Hait, D.; Horn, P. R.; Jacobson, L. D.; Kaliman, I.; Kussmann, J.; Lange, A. W.; Lao, K. U.; Levine, D. S.; Liu, J.; McKenzie, S. C.; Morrison, A. F.; Nanda, K. D.; Plasser, F.; Rehn, D. R.; Vidal, M. L.; You, Z. Q.; Zhu, Y.; Alam, B.; Albrecht, B. J.; Aldossary, A.; Alguire, E.; Andersen, J. H.; Athavale, V.; Barton, D.; Begam, K.; Behn, A.; Bellonzi, N.; Bernard, Y. A.; Berquist, E. J.; Burton, H. G. A.; Carreras, A.; Carter-Fenk, K.; Chakraborty, R.; Chien, A. D.; Closser, K. D.; Cofer-Shabica, V.; Dasgupta, S.; De Wergifosse, M.; Deng, J.; Diedenhofen, M.; Do, H.; Ehler, S.; Fang, P. T.; Fatehi, S.; Feng, Q.; Friedhoff, T.; Gayvert, J.; Ge, Q.; Gidofalvi, G.; Goldey, M.; Gomes, J.; González-Espinoza, C. E.; Gulania, S.; Gunina, A. O.; Hanson-Heine, M. W. D.; Harbach, P. H. P.; Hauser, A.; Herbst, M. F.; Hernández Vera, M.; Hodecker, M.; Holden, Z. C.; Houck, S.; Huang, X.; Hui, K.; Huynh, B. C.; Ivanov, M.; Jász, Á.; Ji, H.; Jiang, H.; Kaduk, B.; Kähler, S.; Khistyayev, K.; Kim, J.; Kis, G.; Klunzinger, P.; Koczor-Benda, Z.; Koh, J. H.; Kosenkov, D.; Koulias, L.; Kowalczyk, T.; Krauter, C. M.; Kue, K.; Kunitsa, A.; Kus, T.; Ladjánszki, I.; Landau, A.; Lawler, K. V.; Lefrancois, D.; Lehtola, S.; Li, R. R.; Li, Y. P.; Liang, J.; Liebenthal, M.; Lin, H. H.; Lin, Y. S.; Liu, F.; Liu, K. Y.; Loipersberger, M.; Luenser, A.; Manjanath, A.; Manohar, P.; Mansoor, E.; Manzer, S. F.; Mao, S. P.; Marenich, A. V.; Markovich, T.; Mason, S.; Maurer, S. A.; McLaughlin, P. F.; Menger, M. F. S. J.; Mewes, J. M.; Mewes, S. A.; Morgante, P.; Mullinax, J. W.; Oosterbaan, K. J.; Paran, G.; Paul, A. C.; Paul, S. K.; Pavošević, F.; Pei, Z.; Prager, S.; Proynov, E. I.; Rák, Á.; Ramos-Cordoba, E.; Rana, B.; Rask, A. E.; Rettig, A.; Richard, R. M.; Rob, F.; Rossomme, E.; Scheele, T.; Scheurer, M.; Schneider, M.; Sergueev, N.; Sharada, S. M.; Skomorowski, W.; Small, D. W.; Stein, C. J.; Su, Y. C.; Sundstrom, E. J.; Tao, Z.; Thirman, J.; Tornai, G. J.; Tsuchimochi, T.; Tubman, N. M.; Veccham, S. P.; Vydrov, O.; Wenzel, J.; Witte, J.; Yamada, A.; Yao, K.; Yeganeh, S.; Yost, S. R.; Zech, A.; Zhang, I. Y.; Zhang, X.; Zhang, Y.; Zuev, D.; Aspuru-Guzik, A.; Bell, A. T.; Besley, N. A.; Bravaya, K. B.; Brooks, B. R.; Casanova, D.; Chai, J. D.; Coriani, S.; Cramer, C. J.; Cserey, G.; Deprince, A. E.; Distasio, R. A.; Dreuw, A.; Dunietz, B. D.; Furlani, T. R.; Goddard, W. A.; Hammes-Schiffer, S.; Head-Gordon, T.; Hehre, W. J.; Hsu, C. P.; Jagau, T. C.; Jung, Y.; Klamt, A.; Kong, J.; Lambrecht, D. S.; Liang, W.; Mayhall, N. J.; McCurdy, C. W.; Neaton, J. B.; Ochsenfeld, C.; Parkhill, J. A.; Peverati,

- R.; Rassolov, V. A.; Shao, Y.; Slipchenko, L. V.; Stauch, T.; Steele, R. P.; Subotnik, J. E.; Thom, A. J. W.; Tkatchenko, A.; Truhlar, D. G.; Van Voorhis, T.; Wesolowski, T. A.; Whaley, K. B.; Woodcock, H. L.; Zimmerman, P. M.; Faraji, S.; Gill, P. M. W.; Head-Gordon, M.; Herbert, J. M.; Krylov, A. I. Software for the Frontiers of Quantum Chemistry: An Overview of Developments in the Q-Chem 5 Package. *J. Chem. Phys.* **2021**, *155*, 084801.
- (7) Perdew, J. P.; Burke, K.; Ernzerhof, M. Generalized Gradient Approximation Made Simple. *Phys. Rev. Lett.* **1996**, *77* (18), 3865–3868.
- (8) Parameswaran, R.; Widawsky, J. R.; Vázquez, H.; Park, Y. S.; Boardman, B. M.; Nuckolls, C.; Steigerwald, M. L.; Hybertsen, M. S.; Venkataraman, L. Reliable Formation of Single Molecule Junctions with Air-Stable Diphenylphosphine Linkers. *J. Phys. Chem. Lett.* **2010**, *1* (14), 2114–2119.
- (9) Venkataraman, L.; Klare, J. E.; Nuckolls, C.; Hybertsen, M. S.; Steigerwald, M. L. Dependence of Single-Molecule Junction Conductance on Molecular Conformation. *Nature* **2006**, *442* (7105), 904–907.
- (10) Park, Y. S.; Widawsky, J. R.; Kamenetska, M.; Steigerwald, M. L.; Hybertsen, M. S.; Nuckolls, C.; Venkataraman, L. Frustrated Rotations in Single-Molecule Junctions. *J. Am. Chem. Soc.* **2009**, *131* (31), 10820–10821.
- (11) Prana, J.; Kim, L.; Czyszczon-Burton, T.; Homann, G.; Chen, S.; Miao, Z.; Camarasa-Gómez, M.; Inkpen, M. Lewis-Acid Mediated Reactivity in Single-Molecule Junctions. *J. Am. Chem. Soc.* **2024**, *146* (48), 33265–33275.
- (12) Camarasa-Gómez, M.; Hernangómez-Pérez, D.; Wilhelm, J.; Bagrets, A.; Evers, F. Molecular Transport. *arXiv* **2024**, No. 2411.01680.
- (13) Blum, V.; Gehrke, R.; Hanke, F.; Havu, P.; Havu, V.; Ren, X.; Reuter, K.; Scheffler, M. Ab Initio Molecular Simulations with Numeric Atom-Centered Orbitals. *Comp. Phys. Commun.* **2009**, *180* (11), 2175–2196.
- (14) Lenthe, E. V.; Baerends, E. J.; Snijders, J. G. Relativistic Regular Two-Component Hamiltonians. *J. Chem. Phys.* **1993**, *99* (6), 4597–4610.
- (15) Arnold, A.; Weigend, F.; Evers, F. Quantum Chemistry Calculations for Molecules Coupled to Reservoirs: Formalism, Implementation, and Application to Benzenedithiol. *J. Chem. Phys.* **2007**, *126* (17), 174101.
- (16) Bagrets, A. Spin-Polarized Electron Transport Across Metal–Organic Molecules: A Density Functional Theory Approach. *J. Chem. Theor. Comput.* **2013**, *9* (6), 2801–2815.
- (17) Camarasa-Gómez, M.; Hernangómez-Pérez, D.; Evers, F. Spin–Orbit Torque in Single-Molecule Junctions from Ab Initio. *J. Phys. Chem. Lett.* **2024**, *15* (21), 5747–5753.
- (18) Fatemi, V.; Kamenetska, M.; Neaton, J. B.; Venkataraman, L. Environmental Control of Single-Molecule Junction Transport. *Nano Lett.* **2011**, *11* (5), 1988–1992.
- (19) Gu, M.-W.; Peng, H. H.; Chen, I.-W. P.; Chen, C. Tuning Surface d Bands with Bimetallic Electrodes to Facilitate Electron Transport across Molecular Junctions. *Nature Mater.* **2021**, *20* (5), 658–664.
- (20) Chen, F.; Li, X.; Hihath, J.; Huang, Z.; Tao, N. J. Effect of Anchoring Groups on Single-Molecule Conductance: Comparative Study of Thiol-, Amine-, and Carboxylic-Acid-Terminated Molecules. *J. Am. Chem. Soc.* **2006**, *128* (49), 15874–15881.
- (21) Ahn, S.; Aradhya, S. V.; Klausen, R. S.; Capozzi, B.; Roy, X.; Steigerwald, M. L.; Nuckolls, C.; Venkataraman, L. Electronic Transport and Mechanical Stability of Carboxyl Linked Single-Molecule Junctions. *Phys. Chem. Chem. Phys.* **2012**, *14* (40), 13841.

- (22) Peng, Z.-L.; Chen, Z.-B.; Zhou, X.-Y.; Sun, Y.-Y.; Liang, J.-H.; Niu, Z.-J.; Zhou, X.-S.; Mao, B.-W. Single Molecule Conductance of Carboxylic Acids Contacting Ag and Cu Electrodes. *J. Phys. Chem. C* **2012**, *116* (41), 21699–21705.
- (23) Jones, P. G. Acetato(Triphenylphosphine)Gold(I), [Au(C<sub>2</sub>H<sub>3</sub>O<sub>2</sub>)(C<sub>18</sub>H<sub>15</sub>P)]. *Acta Crystallogr. C Cryst. Struct. Commun.* **1984**, *40* (8), 1320–1322.
- (24) Nitzan, A. Electron Transmission through Molecules and Molecular Interfaces. *Annu. Rev. Phys. Chem.* **2001**, *52*, 681–750.
- (25) Quek, S. Y.; Venkataraman, L.; Choi, H. J.; Louie, S. G.; Hybertsen, M. S.; Neaton, J. B. Amine–Gold Linked Single-Molecule Circuits: Experiment and Theory. *Nano Lett.* **2007**, *7* (11), 3477–3482.
- (26) Zhang, B.; Garner, M. H.; Li, L.; Campos, L. M.; Solomon, G. C.; Venkataraman, L. Destructive Quantum Interference in Heterocyclic Alkanes: The Search for Ultra-Short Molecular Insulators. *Chem. Sci.* **2021**, *12* (30), 10299–10305.
- (27) Venkataraman, L.; Park, Y. S.; Whalley, A. C.; Nuckolls, C.; Hybertsen, M. S.; Steigerwald, M. L. Electronics and Chemistry: Varying Single-Molecule Junction Conductance Using Chemical Substituents. *Nano Lett.* **2007**, *7* (2), 502–506.
- (28) Huang, M.; Zhou, Q.; Liang, F.; Yu, L.; Xiao, B.; Li, Y.; Zhang, M.; Chen, Y.; He, J.; Xiao, S.; Chang, S. Detecting Individual Bond Switching within Amides in a Tunneling Junction. *Nano Lett.* **2021**, *21* (12), 5409–5414.
- (29) Batra, A.; Darancet, P.; Chen, Q.; Meisner, J. S.; Widawsky, J. R.; Neaton, J. B.; Nuckolls, C.; Venkataraman, L. Tuning Rectification in Single-Molecular Diodes. *Nano Lett.* **2013**, *13* (12), 6233–6237.
- (30) Van Der Molen, S. J.; Liao, J.; Kudernac, T.; Agustsson, J. S.; Bernard, L.; Calame, M.; Van Wees, B. J.; Feringa, B. L.; Schönenberger, C. Light-Controlled Conductance Switching of Ordered Metal-Molecule-Metal Devices. *Nano Lett.* **2009**, *9* (1), 76–80.
- (31) Klausen, R. S.; Widawsky, J. R.; Su, T. A.; Li, H.; Chen, Q.; Steigerwald, M. L.; Venkataraman, L.; Nuckolls, C. Evaluating Atomic Components in Fluorene Wires. *Chem. Sci.* **2014**, *5* (4), 1561–1564.